Journal of Magnetic Resonance 212 (2011) 139–148

Contents lists available at ScienceDirect

Journal of Magnetic Resonance

journal homepage: www.elsevier.com/locate/jmr

Monte Carlo simulation and theory of proton NMR transverse relaxation induced by aggregation of magnetic particles used as MRI contrast agents

Quoc Lam Vuong *, Pierre Gillis, Yves Gossuin

University of Mons, Place du Parc 20, 7000 Mons, Belgium

ARTICLE INFO

Article history:
Received 8 March 2011
Revised 14 June 2011
Available online 1 July 2011

Keywords:
NMR relaxation
MRI
Contrast agent
Superparamagnetic
Clustering
Simulation

ABSTRACT

Superparamagnetic particles are widely used in MRI as R_2 contrast agents. In this last decade, different studies have focused on aggregation of superparamagnetic particles for important applications such as multimodal agents. A complete study – via simulations – of the influence of aggregation on the MR efficiency of these particles at high magnetic field is presented here. First, an empirical expression is proposed for R_2 in the presence of uniformly distributed nanoparticles, taking into account two regimes at once (motional averaging and slow motion regimes). Three cluster shapes are simulated: Sphere, shell and line. An analytical model is proposed to understand water transverse relaxation induced by spherical and shell aggregates. Simulations lead to the conclusion that, in the motional averaging regime, the most efficient aggregate contrast agent is the densest sphere or shell.

© 2011 Elsevier Inc. All rights reserved.

1. Introduction

Since the pioneering work of Néel [1], superparamagnetic (SPM) nanoparticles have been used in a wide variety of applications, such as magnetic storage media [2], medical applications [3,4] or contrast agents [5]. Thanks to their great magnetization, SPM nanoparticles induce great variations in the proton relaxation times that are known to influence magnetic resonance image (MRI) contrast. A complete understanding of this phenomenon in the case of uniform distributions of ultra-small nanoparticles has been reached by Roch et al. [6]. For higher radii, several computational and analytical models describe the transverse relaxation time process at high fields (see for example Refs. [7,8]).

In the last decade, several research projects have focused on the synthesis of aggregates of SPM nanoparticles [9]. These can be useful as MRI-detectable sensors [10]: chemical or biological phenomena can induce aggregation of functionalized SPM particles, modifying the relaxation rates, which can be observed using MRI. On the other hand, several cluster shapes have been synthesized by different groups: a linear shape that allows a better targeting of tumor cells [11,12], a shell shape that can be used as a sensor of drug delivery [3,13] and a spherical shape for use as an MRI sensor [10,14] or as a T2-enhancer [15]. Clustering also occurs for cells labeled with SPM particles [16] or naturally in human organs [17,18].

It is well known that particle clustering results in relaxation rates that are different from rates influenced by the same amount of bare particles [19], but no analytical theory has yet been put forth that is able to predict those modifications. Computer simulations for linear and spherical clustering have been presented, but their results were not confronted with relaxation models [20,21].

The aim of this work is to use Monte Carlo simulations to study transverse relaxation dependence with aggregation of SPM nanoparticles. We propose a unique empirical formula that is able to predict R_2 for a uniform distribution of SPM particles and for a set echo time. Three different clustering shapes are then studied: spherical, shell and linear shapes. Simulation results are compared to analytical models for the sphere and shell cases, which makes it possible to determine the most efficient aggregated contrast agent. A short discussion about the influence of echo time and a comparison with experimental studies are also made.

2. Theory

Relaxation rates are explained by the magnetic field inhomogeneities produced in the sample [22] – in our case, those created by the dipolar magnetic field of the SPM particles. At high static magnetic fields, the relaxation is caused by the local dephasing of each proton spin as it diffuses around the magnetic particles, within the field inhomogeneities.

The equations predicting the induced relaxation rates are unfortunately not general and are only valid under precise conditions

Abbreviations: SPM, superparamagnetic; MRI, magnetic resonance imaging; NMR, nuclear magnetic resonance; FID, free induction decay.

* Corresponding author. Fax: +32 65373537.
E-mail address: quoc-lam.vuong@umons.ac.be (Q.L. Vuong).

1090-7807/$ - see front matter © 2011 Elsevier Inc. All rights reserved.
doi:10.1016/j.jmr.2011.06.024

Nomenclature

f	volume fraction	μ_0	the vacuum magnetic permeability
R	single superparamagnetic particle radius	$\tau_D = R^2/D$	diffusion correlation time
D	water diffusion coefficient	τ_{CP}	the echo time
γ_I	proton gyromagnetic ratio	R_{Agg}	spherical aggregate or shell radius
B_{eq}	superparamagnetic particle equatorial field	d	linear aggregate interparticle distance
N_{SPM}	the number of SPM particles in the sample	N_{Agg}	number of single SPM particles in one aggregate

limiting the possible range of SPM parameters (such as radius and magnetization, for example). A summary of the different models introduced in this section can be found in the first part of table 1.

2.1. Motional averaging regime and outer-sphere theory

The motional-averaging regime can be applied for ultra-small superparamagnetic particles [6]. All SPM characteristics have to be taken into account: Néel time, anisotropy energy, SPM radius and magnetization. At high fields, magnetization is locked and outer-sphere theory predicts for R_2 a quadratic dependence with the SPM radius [8]

$$R_2 = \frac{16}{45} f \frac{R^2}{D} (\gamma_I B_{eq})^2 \tag{1}$$

where R is the SPM radius, D is the translational diffusion coefficient of protons, f is the volume fraction occupied by the SPM particles, defined by $f = N_{SPM}(4\pi R^3/3)/V_{sample}$ where N_{SPM} is the number of SPM particles in the sample of volume V_{sample}, γ_I is the proton gyromagnetic ratio. We suppose the magnetic moment of a magnetite particle proportional to its volume and define B_{eq}, the equatorial field, as

$$B_{eq} = \frac{\mu_0}{4\pi} \frac{\mu_S}{R^3} = \frac{\mu_0}{3} M_s \tag{2}$$

where μ_0 is the vacuum magnetic permeability, μ_S is the magnetic moment of the SPM particle and M_S the bulk magnetization of magnetite. Sometimes, the equatorial field parameter is defined from the root mean square magnetic field at the edge of the particle, which amounts to multiplying definition (2) by a prefactor $\sqrt{4/5}$. For magnetite, the equatorial field is about 0.16 T. Eq. (1) can be applied in the motional averaging regime, i.e. only if the Redfield condition is fulfilled

$$\gamma_I B_{eq} \tau_D < 1 \tag{3}$$

where $\tau_D = R^2/D$ is the diffusion correlation time. Eq. (1) is still valid for a CPMG sequence if the echo time is greater than τ_D, which will be assumed in usual simulations.

2.2. Slow-motion regime and partial refocusing model

When condition (3) is not met, i.e., for large SPM radii, R_2^* can be described by the static model [23,24]

$$R_2^* = \frac{2\pi}{3\sqrt{3}} f \gamma_I B_{eq} \tag{4}$$

This result was obtained under the assumption that the protons are almost motionless in the sample, which means in practical terms that their displacement during a diffusion correlation time τ_D must be much smaller than the proton Larmor frequency induced near the SPM surface. This theoretically leads to the condition

$$\gamma_I B_{eq} \tau_D \gg 1. \tag{5}$$

The rate predicted by the static dephasing model is the maximum R_2 that can be reached for fixed volume fraction and equatorial field. When echoes are applied, a partial refocusing model can be used [8]

$$R_2 = 2.25 \frac{x^{1/3}}{\tau_D} [1.34 + fx]^{5/3} \tag{6}$$

where we introduced the dimensionless factor $x = \sqrt{4/5}\gamma_I B_{eq} \tau_{CP}$, τ_{CP} as the echo time. However, the partial refocusing model supposes that a major region in the sample obeys a local Redfield condition (see the "outer Region" section in Ref. [8]), which requires that an upper bound be imposed to the equatorial field. That requirement results in another condition complementary to relation (5):

$$f \gamma_I B_{eq} \tau_D \ll 1. \tag{7}$$

2.3. Exchange model

Swift and Connick [25] expressed the modification of the relaxation rates in the case of exchange of protons between N different subsystems, each having its own specific relaxation rate R_{2n}. If the large majority of protons belong to the subsystem 1, if τ_n is the exchange time from subsystem n to subsystem 1, and if $\tilde{\tau}_n$ is the

Table 1
Summary of the different models presented in this study and their corresponding conditions and equations. The equations of the second part of the table can only be used with $D = 3 \times 10^{-9}$ m^2/s and inter-echo time of 1 ms.

Model name	Eqs.	Conditions	Comments
Outer-sphere	(1)	$\gamma_I B_{eq} \tau_D < 1$	Exact theoretical model
Static	(4)	$\gamma_I B_{eq} \tau_D \gg 1$	Exact theoretical model; equation for R_2^*
Partial refocusing	(6)	$\gamma_I B_{eq} \tau_D \gg 1$ $f\gamma_I B_{eq} \tau_D \ll 1$	Exact theoretical model
Exchange	(8)		Exact theoretical model
Uniform distribution	(14)		Empirical equation
Spherical-shell clusters	(17) with (18), (23), and (24)		Semi-empirical equation

exchange time from subsystem 1 to subsystem n, the total transverse relaxation rate is given by

$$R_2 = R_{21} + \sum_{n=2}^{N} \frac{1}{\tilde{\tau}_n} \frac{R_{2n}^2 + R_{2n}/\tau_n + \delta\omega_n^2}{(R_{2n} + 1/\tau_n)^2 + \delta\omega_n^2}. \quad (8)$$

$\delta\omega_n$ is the mean frequency difference between subsystems 1 and n.

2.4. Linear clusters

There is no general analytical model for finite linear clusters. Several papers deal with infinite clusters, mainly in order to predict the relaxation induced by blood vessels in MRI. Simulations [26–29] account for realistic values of the vessel parameters [28]. Other research is based on analytical results but with straightforward conditions: Kennan et al. supposed that vessels are perpendicular to the magnetic field [27], Sukstanskii and Yablonskiy proposed interesting expressions based on a Gaussian approximation for the spatial magnetic field correlation, but these were only valid for relatively high volume fractions or for low magnetization [30]. Kiselev and Posse [31] also elaborated analytical expressions but the free induction decay (FID) has to be described by a more complex decay than a simple exponential.

3. Methods

3.1. Simulation steps

Monte Carlo simulations were carried out in order to predict R_2 during a CPMG sequence at a high magnetic field. In theory, the obtained results would only be valid for infinite fields but in practise the field must be high enough for R_2 to saturate. This happens when $\gamma_I B_0 \tau_D > 1$ which is verified for static fields larger than 1 T in case of more-than-5 nm magnetite particles.

Several descriptions of the simulation method may be found in the literature (see Refs. [8,20,21] for example). The algorithm is composed of three main steps:

(1) The SPM distribution is randomly defined, eventually with some shape constraints.
(2) Water proton spins diffuse within the system and their dephasing is calculated.
(3) The FID decay is calculated from the evolution of the mean value of the magnetic moment component that produces the signal.

The simulation space is composed of a central cubic space whose dimension is determined by the volume fraction and the number of SPM particles simulated. The SPM particles are supposed to be impenetrable and immobile during the water proton diffusion. Indeed, the movement of the SPM particle can be neglected. The Stokes–Einstein relation predicts that the diffusion coefficient of a particle in a fluid is inversely proportional to its radius. As the water molecule radius is at least 100 times smaller than the nanoparticles size, the SPM particle diffusion coefficient is 100 times smaller than the water one. To avoid border effects due to the finite number of particles, periodicity is used: the entire simulation space is composed of 27 identical cubes. Fifty aggregates are always simulated in the central cube. Consequently, 27×50 aggregates are distributed in the entire system. The number of SPM particles in the central cube depends on the number of particles that constitute an aggregate. An overlap between adjacent aggregates is allowed. The aggregate generation algorithm will be described in the next sections.

Random walk simulates water proton translational movements amongst randomly distributed SPM particles; at each time step $t_n = n\Delta t$ (where n is an integer), the corresponding water proton position is determined by adding a random step $\vec{\delta}_n$ to the previous position:

$$\vec{r}(t_n) = \vec{r}(t_{n-1}) + \vec{\delta}_n \text{ with } |\vec{\delta}_n| = \sqrt{6D\Delta t} \quad (9)$$

$\vec{\delta}_n$ is a randomly-oriented vector on a sphere whose radius is $\sqrt{6D\Delta t}$. The initial position $\vec{r}(t_0)$ is placed randomly in the central cube. Two tests are necessary to validate the $\vec{r}(t_n)$ position:

(1) SPM particles are assumed to be impenetrable, so any jump leading to the positioning of the water proton inside a magnetic particle is prohibited.
(2) If $\vec{r}(t_n)$ is located outside of the central cube, it is instantaneously relocated to the position corresponding to the opposite face of the cube.

During the diffusion, at a high static field, defined as aligned along the z-axis, the local magnetic field felt by the proton spin induces a local Larmor precession of its magnetic moment, which results in a rotation in the xy-plane, i.e., a dephasing. This dephasing is proportional to the z-component of the local magnetic field felt by the proton, which is itself the sum of all dipolar magnetic fields produced by the SPM particles:

$$B_{tot}(\vec{r}) = \sum_{\substack{i=SPM \\ particles}} B_{loc}(r_i, \theta_i); \quad B_{loc}(r, \theta) = R^3 B_{eq} \frac{3\cos^2\theta - 1}{r^3} \quad (10)$$

where R is the SPM radius, r is the distance between the proton spin and the SPM particle being considered and θ the inclination angle of the vector joining the proton spin to the SPM particle. Thus the dephasing for the jth proton spin is given by

$$\Delta\phi_n^j = \gamma_I B_{tot}(\vec{r}_j(t_n))\Delta t \quad (11)$$

where $\vec{r}_j(t_n)$ is the position of the jth proton spin at time t_n. For an initial pulse around the y-axis in the rotating frame, the normalized transverse magnetic moment of the jth water proton in the rotating frame is thus

$$\vec{\mu}_j(t_n) = (\cos\phi_n^j, \sin\phi_n^j, 0) \quad (12)$$

with $\phi_n^j = \phi_{n-1}^j + \Delta\phi_n^j$ and $\phi_0^j = 0$. If an echo-pulse is applied at time t_n along the x-axis, the phase ϕ_n^j has to be replaced by $-\phi_n^j$. This simulation considers the water proton spin as a classical vector which has to be considered as the average of the quantum proton spin operator. The magnetic moment $\vec{\mu}_j$ must rigorously be interpreted as the average spin of a pack of protons following the same diffusion trajectory.

The normalized FID is then reconstructed by taking the modulus of the transverse magnetic moment average over all the N_{protons} proton spins for each t_n:

$$\langle\mu(t_n)\rangle = \frac{1}{N_{\text{protons}}} \sqrt{\left(\sum_{j=\text{protons}} \cos\phi_n^j\right)^2 + \left(\sum_{j=\text{protons}} \sin\phi_n^j\right)^2}. \quad (13)$$

The resulting FID is then fitted by a mono-exponential, giving the simulated R_2. If the corresponding reduced chisquare is greater than 0.0001, a double-exponential is used and R_2 is given by the relaxation rate of the mode with the largest amplitude.

3.2. Grid optimization

In order to spare computation time, the local magnetic field of the SPM particles is pre-calculated at every node of a $200 \times 200 \times 200$ grid before the proton diffusion step. The local magnetic field is then calculated thanks to a tri-linear approximation, at least when the proton is relatively far from the

SPM particles. Otherwise, when the distance from the proton to the closest SPM particle is less than 10 nodes, the local field is calculated exactly. The contribution due to distant SPM particles is then added thanks to the tri-linear approximation of the grid.

3.3. Parameters

The physical parameters of the simulations are:

- The diffusion coefficient of water at 310°K: $D = 3 \times 10^{-9}$ m^2/s.
- The equatorial field of magnetite: B_{eq} = 0.16 T corresponding to a saturation magnetization of 100 Am^2/kg [Fe].
- A volume fraction f of 3.14×10^{-6} (as in Ref. [20]). With this volume fraction, the relaxivity (defined in Section 4) can be obtained by taking 4.74 times the simulated relaxation rate.
- An inter-echo time (time between two 180° pulse) of $2\tau_{CP} = 1ms$.

The simulation parameters are:

- Number of aggregates in the total simulation space: 50×27.
- Random jumps: $|\vec{\delta}_n| = R$ (where R is the SPM radius) if the distance between all the SPM particles and the proton is greater than $8R$ and $|\vec{\delta}_n| = R/8$ if at least one SPM particle is nearer than $8R$ from the proton. This adaptive space step allows us to take into account the fact that variations in magnetic field near the SPM particles are greater than far away from them, which also makes the computation faster. The relation (9) makes it possible to deduce the corresponding time steps.
- Number of protons : from 5000 to 20,000.

For each set of parameters, three different simulations are made: each reported data point is the mean of three simulated R_2 and error bar corresponds to twice the standard deviation.

3.4. Aggregate generation

Three types of aggregates were studied: linear, spherical and spherical shell aggregates (see Fig. 1). Each one is characterized by several parameters and the aggregate generation method depends on its shape:

- A constant number of SPM particles is determined.
- The orientation of linear aggregates is generated randomly and the inter-particle distance is d.
- For spherical aggregates, a radius R_{Agg} is chosen by the user. SPM positions are defined randomly with the condition that they have to be in the sphere of radius R_{Agg} and that the SPM particles are impenetrable to each other.
- For highly dense spherical aggregates, the generation is slightly different: the aggregate is filled up with particles layer by layer, and the layer thickness is equal to the particle diameter.

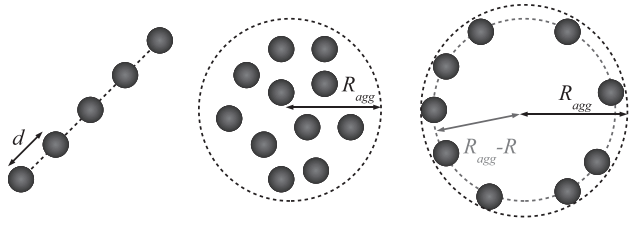

Fig. 1. The three different shapes of simulated aggregates (linear, spherical and spherical shell) and their geometrical parameters. These are obviously the 2D versions of the simulated aggregates.

- For spherical shell aggregates, a shell center is defined. SPM particles are randomly placed on the surface of the shell, so that each particle has its center situated at a well-defined distance from the shell center, i.e., $R_{Agg} - R$.

3.5. Hardware

All routines were written in C++, parallelized with OPENMP, used the Gnu Scientific Library (GSL), compiled with the Intel C++ Compiler and run on Linux systems. Simulations were performed on desktop computers and on resources of the *Interuniversity Scientific Computing Facility* located at the University of Namur and of the *Service Général d'Informatique* (SEGI) at the University of Liège.

4. Results and discussion

Four different spatial configurations of SPM particles were studied: the well-known uniform case, the spherical aggregate, the shell and the linear geometry. Fig. 1 illustrates these systems and their respective parameters. The present discussion aims to understand the relaxation induced by these systems and to determine the most efficient contrast agent. The new models introduced in this work are summarized in the second part of Table 1.

The efficiency of a contrast agent depends on the relaxivity r_2, namely the relaxation rate increase induced by a 1 mM/L increase of iron concentration of the sample: the higher r_2 is, the more efficient the contrast agent is. Indeed, in an R_2 MRI sequence, the greatest variation of the transverse relaxivity leads to the highest contrast modification. Our simulations used a constant volume fraction and, consequently, give an R_2 that is proportional to r_2: our different simulations can be compared to each other from the efficiency point of view.

4.1. Uniform distribution of single SPM particles

The case of a uniform distribution of single SPM particles is studied first. Generating such a distribution is easy: the particles are randomly disposed in the simulation space, taking into account they are impenetrable. In order to avoid aggregation of particles, a supplementary condition is introduced: the distance between two SPM particles has to be larger than 20 times their radius.

The classical dependence of the transverse relaxation rates with the SPM radius is reproduced (Fig. 2): the increasing part of the curve is related to the outer-sphere regime and the decreasing one to the static dephasing regime. The different models fit the curve well in their respective validity region: the outer-sphere theory is confirmed for radii smaller than 10 nm, i.e., the radius corresponding to Redfield's condition (3), the maximum rate reached for a 20-nm radius is in accordance with the value of 163 s^{-1} predicted by the static model (Eq. (4)) and the third part is well described by the partial refocusing model (Eq. (6)) for sufficiently large radii.

That global agreement with pre-existing models can be improved by introducing an empirical equation that can match the relaxation behavior within the three regimes considered so far, for a uniform SPM particle distribution (the parameters were all defined previously):

$$R_2^{\text{unif}}(R, B_{\text{eq}}, f) = f \frac{(a \times B_{\text{eq}} \times R)^2}{1 + b \times R \times B_{\text{eq}}^{\alpha} + \left(c \times R \times B_{\text{eq}}^{\alpha}\right)^2 + \left(d \times R \times B_{\text{eq}}^{\alpha}\right)^3 + (e \times R \times B_{\text{eq}}^{\alpha})^4}, \tag{14}$$

where $\alpha = 0.42$, $a = 2.5209 \times 10^{12}$, $b = -0.1177 \times 10^{9}$, $c = 0.1295 \times 10^{9}$, $d = 0.0523 \times 10^{9}$ and $e = 0.0566 \times 10^{9}$ are empirical parameters, expressed in SI units. As shown in Fig. 2, this expression perfectly fits the simulation results for radii ranging from 2.5 nm to 300 nm and for B_{eq} below 0.16 T (not shown).

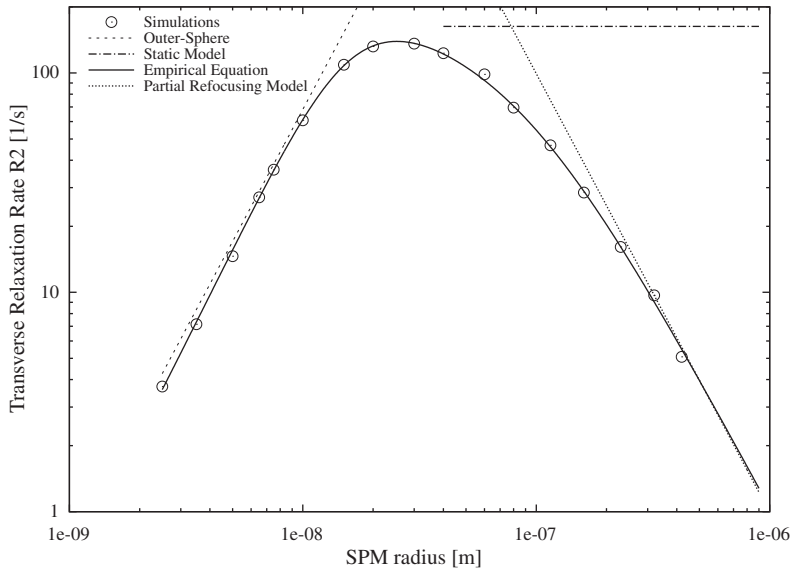

Fig. 2. SPM radius dependence on R_2 in the uniform distribution case. Parameters used are given Section 3.3: $D = 3 \times 10^{-9}$ m^2/s, $f = 3.14 \times 10^{-6}$. The different models shows a good fit with the points in the region where they are valid. The curve given by empirical Eq. (14) is also shown.

Within the validity domain of the Redfield condition, Eq. (14) predicts a quadratic dependence of R_2 with RB_{eq}, as does the outer-sphere model (see Eq. (1)). For large radii, Eq. (14) is characterized by the same R_2 dependence on radius, as in the partial refocusing model. However, there is a difference between Eq. (14) and the partial refocusing model concerning their dependence with B_{eq}, but the validity of the partial refocusing model is conditioned by fulfilling condition (7), which imposes an upper bound to the possible values of B_{eq}. We will thus use Eq. (14) as a valid empirical description of the transverse relaxation for the simulated rates for the physical parameters set in the Section 3.3 (namely diffusion coefficient and interecho times).

4.2. Spherical aggregates

For spherical aggregates, we screened three parameters: the number N_{Agg} of SPM particles in one aggregate, the aggregate radius R_{agg} and the SPM particle radius R.

4.2.1. Number of particles in one highly dense aggregate

The R_2 dependence with the number of particles in one aggregate on R_2 is shown in Fig. 3: for SPM particles small enough to validate the motional averaging regime, R_2 increases with N_{Agg} comprised between 1 and 100. The spherical aggregates are highly dense (see Section 3). For this type of aggregate, Ref. [21] mentions $R_2 \propto N_{Agg}^{0.44}$. A fit of our data for the 5 nm particles with a power law yields$R_2 \propto N_{Agg}^{0.40}$, which is in good agreement with those results. Following the fractal analysis of Shapiro et al. [32], $R_{Agg} \propto RN_{Agg}^{1/\xi}$ where $\xi = 2.2$ is the fractal dimension of the aggregates, which leads to conclude that $R_2 \propto N_{Agg}^{\alpha}$, with α between 0.18 and 0.55. Our result lies within that range.

Another way to predict how highly dense aggregates will influence R_2 is to consider the aggregate as a single larger particle, with values of the equatorial field, of the radius and of the volume fraction adjusted to the aggregate configuration. The main problem is to define the right effective radius of the aggregate: the highly dense aggregate generation method does not lead to a precise definition of the aggregate radius. If the aggregate is completely filled with SPM particles, with no region for water to diffuse in it, the effective radius $\tilde{R}_{Agg}$ could be defined from the total volume of SPM particles in the aggregate – such as $4\pi\tilde{R}_{Agg}^3/3 = N_{Agg}4\pi R^3/3$, as suggested in Ref. [19]. Unfortunately, when two particles are next to each other, the total aggregate volume is not fulfilled: considering that the optimal density is obtained when a sphere of radius R occupies a cube of $2R$ side length, the effective aggregate volume occupied by N_{Agg} particles would be $N_{Agg}(2R)^3$, the effective radius of the spherical aggregate then being

$$\tilde{R}_{Agg} = R\sqrt[3]{6N_{Agg}/\pi} \tag{15}$$

with the effective volume fraction and equatorial fields (see (2) and definition of f)

$$\tilde{f} = 6f/\pi; \quad \tilde{B}_{eq} = \pi B_{eq}/6. \tag{16}$$

The R_2 corresponding to the aggregate can then be obtained by replacing these values in Eq. (14). The corresponding curves are shown in fig 3 and fit the simulation results very well. For the largest aggregate, R_2 is underestimated – certainly because when the aggregate becomes very large, it also becomes more and more difficult to generate the densest aggregate. Dense aggregates can thus, as expected, be considered as a single SPM particle, if their parameters are chosen adequately.

The advantage of expression (14) is that it is valid in the static dephasing regime. A single procedure was thus applied for all aggregates, including those containing 230 nm particles; Fig. 3 shows that Eq. (14) fits the simulation points.

4.2.2. Influence of the radius aggregate

Fig. 4 shows the R_2 dependence on the aggregate radius when $N_{Agg} = 50$ and the particle radius are kept constant (see other materials A1 and A2 for $N_{Agg} = 6$ or 15). Results are similar to previously published results [20]. Three behaviors can be observed, depending on the particle radius. These can be qualitatively understood by considering the aggregate as a single particle with the adapted parameters (16). If this "single particle" and the SPM particles constituting the aggregate are in the motional averaging regime, R_2 decreases with increasing aggregate radii, towards a limit corresponding to the uniform case. Indeed, the highly dense aggregate gives a larger R_2 than does the uniform distribution one in this case (see Fig. 2) and it is expected that when R_{Agg} is very large, the obtained R_2 value corresponds to the uniform case. An analog reasoning can be made for the slow motion regime leading to an increase of R_2 with the aggregate radius, which is indeed observed.

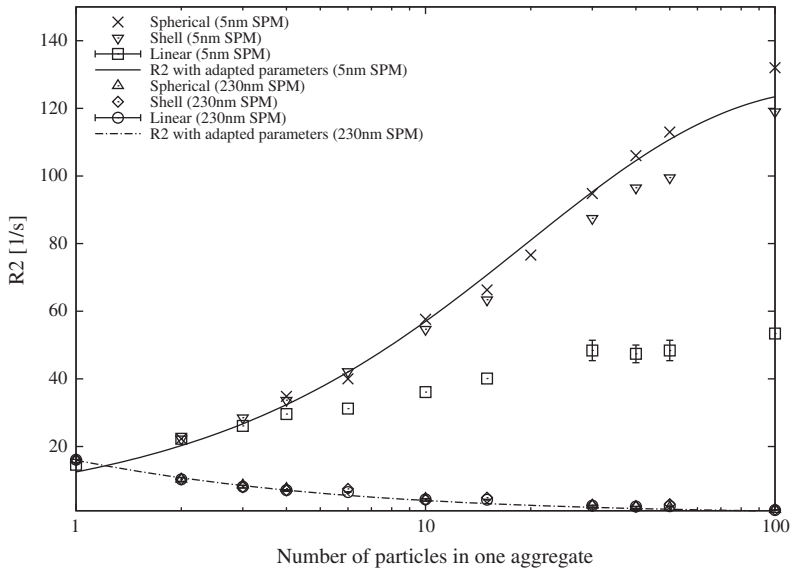

Fig. 3. R_2 of different aggregate shapes and two different SPM particle radiuses. The aggregates are generated to be as dense as possible. Simulation parameters used: $D = 3 \times 10^{-9}$ m^2/s, $f = 3.14 \times 10^{-6}$. The curves are plotted with Eq. (14) by taking the adapted radius (15), equatorial field and volume fraction (16), considering the aggregate as a single magnetized particle.

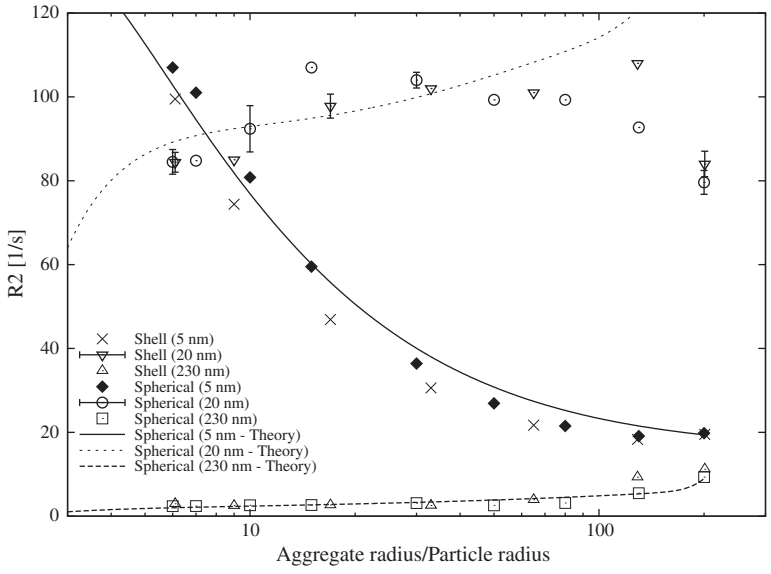

Fig. 4. Simulated results for spherical and shell aggregates of 50 particles. Simulation parameters used: $D = 3 \times 10^{-9}$ m^2/s, $f = 3.14 \times 10^{-6}$. Curves are traced with Eq. (25). Error bars are not shown when they are smaller than their corresponding point size.

However, this cannot explain the behavior for the intermediate case, in which R_2 seems to be constant.

To quantitatively understand the simulation results, considering the aggregate as an impenetrable single particle is not enough: water diffusion in the aggregate (inner-aggregate region) and exchange with bulk water has to be taken into account, as represented in Fig. 5. Considering Eq. (8), the relaxation rate of the aggregate is thus the sum of two contributions (the bulk and the exchange ones)

$$R_{2\mathrm{Agg}} = R_{2\mathrm{Bulk}} + R_{2\mathrm{Exchange}} \tag{17}$$

The bulk term consists in considering the aggregate as an impenetrable sphere with a radius equal to R_{Agg} that is magnetized by its magnetic inner-particles, assuming that the most abundant system is the bulk around the aggregate. Again, Eq. (14) can then be used with the appropriate parameters

$$f_{bulk} = \frac{f}{N_{\mathrm{Agg}}}\left(\frac{R_{\mathrm{Agg}}}{R}\right)^3; \quad B_{\mathrm{eq\ Bulk}} = N_{\mathrm{Agg}} B_{\mathrm{eq}}\left(\frac{R}{R_{\mathrm{Agg}}}\right)^3;$$

$$R_{2\mathrm{Bulk}} = R_2^{\mathrm{unif}}\left(R_{\mathrm{Agg}}, B_{\mathrm{eq\ Bulk}}, f_{\mathrm{Bulk}}\right). \tag{18}$$

The exchange term is not as easy to calculate with Eq. (8): there are no explicit exchange sites in the aggregate, because the protons are assumed to freely diffuse in it. Roch et al. [19] proposed an ingenious mathematical model to adapt the exchange model with free inner-aggregate diffusion. The main idea is to use the diffusion equation:

$$\frac{\partial W(\vec{r},t)}{\partial t} = D\Delta W(\vec{r},t) \tag{19}$$

with initial conditions

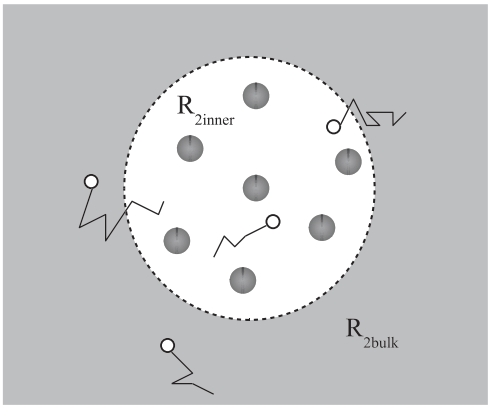

Fig. 5. Diffusion of water protons in the spherical low density aggregate. Two environments with their own relaxation rate are identified: the bulk and the inner-aggregate regions. The proton exchange between these regions leads to the measured relaxation rate R_2.

$$W(\vec{r},0)=\begin{cases}0 \text{ if } |\vec{r}|>R_{Agg}\\ 3/(4\pi R_{Agg}^3) \text{ if } |\vec{r}|<R_{Agg}\end{cases} \tag{20}$$

signifying that the proton is initially situated within the aggregate. $W(\vec{r},t)$ is the conditional probability density for the proton to be in position $\vec{r}$ at time t supposing that it was initially in the aggregate. The solution to this equation is given by:

$$W(\vec{r},t)=\frac{3}{2\pi R_{Agg}R_e|\vec{r}|}\sum_{n=1}^{\infty}B_n\sin(n\pi|\vec{r}|/R_e)e^{-n^2\pi^2Dt/R_e^2}, \tag{21}$$

where $R_e=R_{Agg}(\pi/6f_{Bulk})^{1/3}$ is half the mean distance between two aggregates, $B_n=(\sin\alpha_n/\alpha_n-\cos\alpha_n)/\alpha_n$, $\alpha_n=n\pi R_a/R_e$. Integrating $W(\vec{r},t)$ over a sphere of radius R_{Agg} gives

$$W(t)=\sum_{n=1}^{\infty}p_ne^{-t/\tau_n} \tag{22}$$

where $p_n=6R_{Agg}B_n^2/R_e$ and $\tau_n=R_e^2/(n^2\pi^2D)$. Roch et al. [19] interpreted each term of this sum as the decay of a virtual water fraction p_n coming from the (also virtual) nth site. Thus, the exchange between the aggregate and the bulk can be seen as an exchange between an infinite number of sites, each one characterized by its water fraction (p_n) and its own decay time (τ_n). Eq. (8) can then be used to calculate the exchange contribution to relaxation rates: at equilibrium, decay times must obey the relation $p_{Bulk}/\tilde{\tau}_n=p_{inner}p_n/\tau_n$ (where $p_{Bulk}=\left(R^3f^{-1}-R_{Agg}^3\right)/\left(R^3f^{-1}-N_{Agg}R^3\right)\approx 1$ and $p_{inner}\approx\left(R_{Agg}^3-N_{Agg}R^3\right)/\left(R^3f^{-1}-N_{Agg}R^3\right)$ are respectively the bulk and the inner-aggregate proton fraction). In these conditions, the exchange rate term corresponds to

$$R_{2Exchange}=\sum_{n=1}^{\infty}\frac{p_{inner}p_n}{\tau_n}\frac{R_{2inner}}{(R_{2inner}+1/\tau_n)}, \tag{23}$$

It can be noted that, in our case, the mean frequency shift is equal to zero which is a property of the dipolar interaction. To be complete, the inner-aggregate relaxation rate has to be determined. Eq. (14) is again used with modified parameters

$$f_{inner}=\frac{N_{Agg}R^3}{R_{Agg}^3};\quad B_{eq\ inner}=B_{eq};\quad R_{2inner}=R_2^{unif}(R,B_{eq\ inner},f_{inner}). \tag{24}$$

Finally, Eqs. 17, 18, 23, and 24 allow computation of the total aggregation transverse relaxation rates.

The infinite sum (23) was computed with N terms such as $\sum_{n=1}^{N}p_n\geqslant 0.99$. The obtained curves are presented in Fig. 4. It can be observed that they fit quantitatively well the different results for particles in the motional-averaging and the slow motion regimes and qualitatively reproduce the constancy of the intermediate regime. The difference between simulation points and theoretical curves in this regime could be explained by the fact that the region is the boundary between a mono-exponential and a double-exponential behavior of the FID and that this is also the limit where the echoes start to be efficient. That makes the algorithm more sensitive to small aggregate spatial configurations and thus, the obtained R_2 may present large uncertainties.

A simpler expression can be used instead of Eq. (23) if fast exchanges occur ($\tau_{N=1}\ll T_{2inner}$), as in the case of aggregates of 5 nm particles. In that case, expression (23) leads to

$$R_{2Agg}=p_{Bulk}R_{2Bulk}+p_{inner}R_{2inner}, \tag{25}$$

and the relaxation rate is simply the mean rate of the bulk and the inner regions. This has been confirmed with 5 nm particles (not shown). The exchange terms are not negligible for larger SPM radii, especially in the slow motion regime.

4.3. Shell aggregates

"Highly dense" shell aggregates were generated: due to the generation procedure, based on a random determination of the SPM positions, it was not possible to fill the whole spherical surface. A ratio range, defined as $N_{Agg}4\pi R^2/\left(4\pi R_{Agg}^2\right)$, from 50% to 60% was obtained for the aggregates simulated in Fig. 4.

As can be observed in Figs. 3 and 4, the simulated points (even for the other radii and other numbers of particles) for shell aggregates are equivalent to the corresponding spherical aggregate – assuming that a shell can be considered as a spherical aggregate with radius R_{Agg}. The simulations show that for the studied range of radii (from 5 nm to 230 nm), all the simulated shells can be assimilated to the corresponding spherical aggregates with the same radius for a range from 2 to 100 particles.

A more precise observation of the curves from Fig. 4 shows slight differences for aggregates with small radii and small SPM particles. This can be qualitatively understood by the fact that for shell aggregates, particles have to be on the sphere surface which does not allow "inner-aggregation" in the center of the shell that could enhance the relaxation in the outer-sphere regime.

4.4. Linear aggregate

Results on linear aggregates significantly differ from those obtained for the spherical and shell clusters in the motional-averaging regime. As can be seen in Fig. 3, the linear curve seems to split from the spherical one for aggregates containing six 5 nm-particles. On the other hand, the shape does not seem to influence relaxation rates in the slow motion regime. A more detailed comparison between the different shape behaviors will be made in Section 4.5.

Different linear aggregate parameters were studied, such as the inter-particle distance d or the orientation of the linear aggregates and our results confirm previously published ones [20,21] : as in Ref. [20], in which aggregates of 6 and 15 particles were simulated, the two relaxation regimes led to different behaviors. In the motional averaging regime, a decrease of R_2 is observed when the inter-particle distance increases, while in the slow motion regime, R_2 increases with distance. In the intermediate regime, the dependence of R_2 on the distance is very weak. As an example, the curves obtained for aggregates of 50 particles are presented in fig 6.

The linear aggregate orientation is important. In Ref. [21], the orientation of linear aggregates of only two particles was studied.

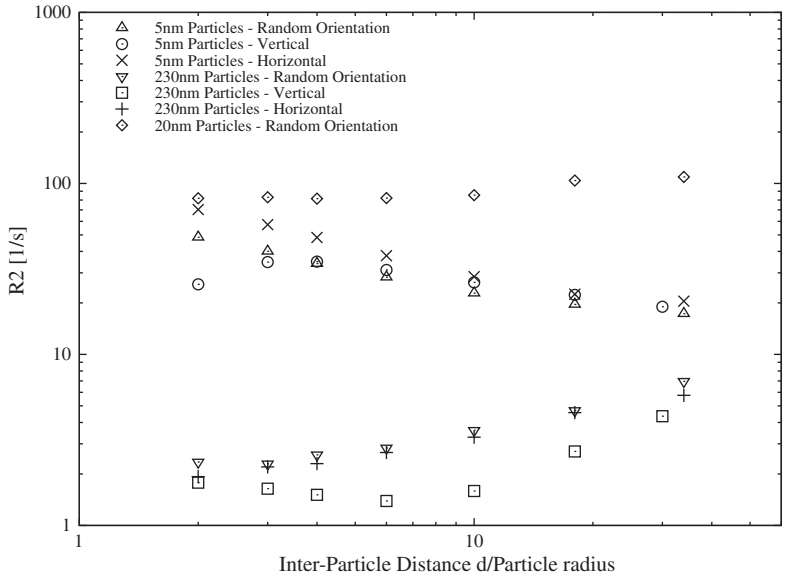

Fig. 6. Simulation results for linear aggregates of 50 SPM particles. Simulation parameters used: $D = 3 \times 10^{-9}$ m^2/s, $f = 3.14 \times 10^{-6}$.

Three types of orientations are studied in the present work (random orientation of the linear aggregates, vertical and horizontal orientations – random and vertical orientations are the most relevant for realistic systems) and the influence of the inter-particle distance is also studied for 5 nm and 230 nm SPM particles. In the motional averaging regime, a non trivial behavior can be observed for vertical orientations in fig 6: the maximum relaxation rate is not observed for the densest aggregate (i.e. when $d = 2$).

Horizontal aggregates are more efficient than vertical and randomly oriented ones in the slow motion regime. This can be understood thanks to the geometry of the dipolar interaction in case of linear aggregates. If the linear aggregate size is infinite and if the magnetic moment is oriented along the cylinder axis (i.e. vertical case), the local magnetic field is zero outside the cylinder [33]. In this case, the relaxation can only occur thanks to boundary effects. In the vertical case, i.e. when the magnetic moment is perpendicular to the cylinder axis, the local field outside the cylinder is non-zero which fastens the relaxation.

These curves can be compared with the results for spherical aggregates if we assign the volume of the cylinder containing the linear aggregate to the corresponding sphere. The two geometrical parameters can then be expressed as

$$\frac{d}{R} = \frac{(R_{\mathrm{Agg}}/R)^3 - 2}{(N_{\mathrm{Agg}} - 1)}. \tag{26}$$

However, with this procedure, the spherical aggregate yields larger relaxation rates (not shown), signifying that a sphere and a cylinder of equal volume are not equivalent from an NMR point of view.

Particle radius is also an important parameter in the obtained relaxation: Fig. 7 shows the SPM radius dependence with the relaxation rates for dense ($d = 2$) linear aggregates of 6, 15 and 50 SPM particles. The obtained curves have similar shapes as in the uniform case, with lower and shifted maximum. For aggregates containing more particles, the maximum is more shifted and its

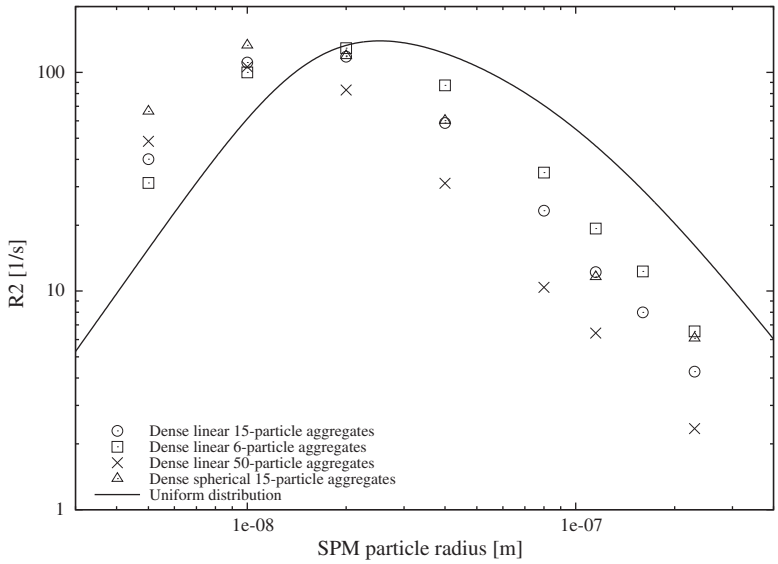

Fig. 7. Simulation results for dense linear (d = 2) aggregates of 6, 15 and 50 SPM particles. Parameters used for all the simulations: $D = 3 \times 10^{-9}$ m^2/s, $f = 3.14 \times 10^{-6}$. Error bars are not shown when they are smaller than their corresponding point size.

amplitude decreases. The shift phenomenon can easily be understood: if the SPM radius is larger, the aggregate "radius" is larger and, thus, the Redfield condition is no longer satisfied. The lower maximum can be attributed to the fact that linear geometry seems to decrease the magnetic gradients generated by the dipolar fields and therefore also decreases the relaxation rates.

4.5. Comparison between linear and spherical aggregates

Fig. 3 offers an interesting comparison of the relaxation rates of the different aggregate shapes. Spheres and spherical shells are equivalent from a magnetic relaxation point of view. Clearly, for highly dense aggregates, in the motional averaging regime and for the same number of SPM particles, relaxation induced by spherical clusters is faster than relaxation induced by linear clusters. For aggregates of 100 particles, a spherical shape gives a relaxation rates that is twice as larger as a linear one. Even for lower density aggregates, when the inter-particle increases, the previous section showed that, for equal volume, the spherical aggregate is still more efficient than the linear one. Fig. 7 also shows that for the densest aggregates, relaxation induced by a spherical aggregate is always the fastest for all SPM radii studied.

On the other hand, in the static dephasing regime, for highly dense aggregates, no significant difference can be observed between the spherical and linear shapes. Fig. 7 shows that for radii larger than 20 nm – the limit between the two regimes – the curves for spherical and linear aggregates of 15 particles match each other. The static dephasing regime thus seems less dependent on the aggregate shape.

4.6. Influence of the inter-echo time

To simplify the discussion, an inter-echo time of 1 ms – which is the usual value in relaxometry – was kept constant for all the simulations. We discuss in this section of the possible variation of the relaxation rates induced by different inter-echo times.

According to outer-sphere theory, a variation of the echo time for aggregate and single particles in the average motional regime should not lead to great changes in the results, if the echo time is greater than the correlation time τ_D. Simulations with inter-echo times of 0.1 ms and 10 ms were carried out for linear aggregates (with geometrical parameters d = 10 and 50 nm), shell aggregates (with R_{Agg} = 25 and 160 nm) and spherical aggregates (with R_{Agg} = 30 and 150 nm) – all composed of 50 particles of 5 nm. The results show variations lower than the error bars.

For particles and aggregates in the slow motion regime, the relaxivities are expected to vary with the echo time. In Ref. [8], it was shown that for an inter-echo times range of 0.1–10 ms, the relaxation times induced by uniform distributions of particles in the slow motion regime could increase by a factor of 10. Simulations also show that this effect is of the same order for linear aggregates (with d = 260 and 2300 nm), shell aggregates (with R_{Agg} = 1150 and 7360 nm) and spherical aggregates (with R_{Agg} = 1380 and 6900 nm) – all composed of 50 particles of 230 nm.

4.7. Comparison with experiments

The simulation results have been compared to experimental data found in three studies focusing on three different configurations: the linear geometry [12], the uniform distribution [34] and the highly dense spherical aggregate [35].

For the linear case, experimental relaxivities r_{2Lexp} of the aggregates were found greater than the corresponding uniform distribution r_{2Uexp} [12]. Our simulations were used in Ref. [12] and led to the right relaxivity ratio r_{2Lexp}/r_{2Uexp} between these two configurations. However, the relaxivities obtained by simulations were significantly smaller than the experimental ones and were attributed to the sample size polydispersity.

Table 2
Relaxivities obtained in experimental studies for different radii and equatorial fields are compared to the relaxivities predicted by our models.

Systems	Radius (nm)	Magnetization (A/m)	Experimental r_2 (s^{-1} mM^{-1})	Theoretical r_2 (s^{-1} mM^{-1})
Uniform distribution [34]	4.2	300,440	54.7	31.1
	4.8	321,160	95.2	47.3
	5.0	321,160	99.5	51.6
Dense spherical aggregates [35]	24.5	72,800	234	277
	29.5	72,800	363	349
	38	72,800	413	427
	56.5	72,800	512	455
	21.5	49,600	117	161

Results from the uniform distribution [34] and their corresponding theoretical values are shown in Table 2. Eq. (14) was used with the adapted radius and equatorial field to predict the theoretical relaxivities. These ones are smaller than the experimental ones – this can be attributed to the polydispersity of the sample: for low radius, the square SPM radius dependence on the relaxivity makes it sensible to the size distribution. Nevertheless, the theoretical results seem to exhibit the right trend: a larger radius induces larger relaxation rates.

Table 2 also shows comparison between experimental and theoretical relaxivities of systems composed of dense spherical aggregates. These systems are obtained by a coating of several single particles [35]: this layer is considered impermeable to water. Consequently, in the theoretical calculus, the exchange term is taken equal to zero in Eq. (17). This leads to a good consistency between experimental and theoretical data.

5. Conclusions: the optimal R_2 contrast agent

The aim of this work was to determine if aggregation of SPM particles could lead to better transverse relaxivities, i.e. more efficient R_2 contrast agents, than single particles. Impact of aggregation shapes and their geometrical parameters on relaxation rates were studied through simulations.

In uniform distribution, relaxation of single SPM particles can be categorized into two regimes according to particle radius: the motional averaging regime and the slow motion regime. An intermediate regime, defined as the limit of the previous ones, occurs at around 20 nm and gives the best relaxivity of 163 s^{-1}, which can be calculated thanks to Eq. (4). The empirical Eq. (14) appears to correctly describe both regimes and the transition between them. In all our simulations, this was the best relaxivity ever reached (for an equatorial field of 0.16 T). Thus, the optimal R_2 contrast agent is a single SPM particle at intermediate regime, with a radius of about 20 nm.

As explained in the introduction, aggregations are sometimes necessary to obtain multimodal agents, which justifies the investigations aimed at determining the most efficient agent in the aggregation state. It is also an easier way to synthesize magnetic entities with a larger radius than synthesizing a mono-crystal.

In the case of aggregation, our discussion starts from clusters made of particles with a given SPM radius. Indeed, according to the studied regime (outer-sphere, slow motion or intermediate), the simulations lead to different conclusions:

(a) In the outer-sphere regime, our work indicates that optimal agents are obtained when the aggregation shape is a sphere (Fig. 3). A linear shape can decrease the relaxivity down to half the value corresponding to the spherical shape. The difference

between shell aggregates and spherical ones is weak, indicating that in the case of liposomes, the SPM particles can be concentrated in the core or at the surface – supposing that the layer is permeable. If the layer is impermeable, the shell shape is probably preferable, because it allows the protons to get nearer to the individual SPM particles. Aggregate density also influences the relaxation rates: the most efficient contrast is obtained for the highest density. Unfortunately, even the highest density cannot produce relaxation rates of the uniform distribution case (around 163 s^{-1}), due to the loss of the overall magnetization of the aggregate.

(b) In the slow motion regime, the conclusions are very different: relaxation is essentially independent from the aggregation shape, and it is preferable to have a density of SPM particles that is as low as possible in order to reach a high relaxivity.

(c) The intermediate regime is the most interesting case from the MRI point of view: it yields the highest relaxivities and does not appear to depend on aggregate shape or density. However, this could be a problem for liposome applications where, for example, drug delivery coincides with a variation of the aggregate density that has to be observed using MRI. In that case, the two previous regimes will provide better results.

Acknowledgments

The authors are grateful to Prof. Francis Moiny for his detailed explanations about the R_2 algorithm, Dr. Alain Roch for his help on the theory of MR relaxation induced by SPM, Michael Hoste and Jorge Pinna-Puissant for their help with algorithm parallelization, Prof. Roberto Lazzaroni, Prof. David Beljonne, Prof. Tom Mens and Dr. David Colignon for providing access to the computation resources. Quoc Lam Vuong acknowledges the F.R.S.-FNRS for financial support.

This research used resources of the *Interuniversity Scientific Computing Facility* located at the University of Namur, Belgium, which is supported by the F.R.S.-FNRS under convention No. 2.461707 and resources of the *SEGI* located at the University of Liège, Belgium.

Appendix A. Supplementary material

Supplementary data associated with this article can be found, in the online version, at doi:10.1016/j.jmr.2011.06.024.

References

[1] L. Néel, Theory of the magnetic after-effect in ferromagnetics in the form of small particles with applications to baked clays, Ann. Geophys. (C.N.R.S.) 5 (1949) 99–136.
[2] N. Spaldin, Magnetic data storage, in Magnetic Materials, Fundamental and Device Applications, Cambridge University Press, Cambridge, 2003, pp. 132–158.
[3] S. Lecommandoux, O. Sandre, F. Chécot, R. Perzynski, Smart hybrid magnetic self-assembled micelles and hollow capsules, Prog. Solid State Chem. 34 (2006) 171–179.
[4] C. Corot, P. Robert, J.-M. Idée, M. Port, Recent advances in iron oxide nanocrystal technology for medical imaging, Adv. Drug Deliv. Rev. 58 (2006) 1471–1504.
[5] Y. Gossuin, P. Gillis, A. Hocq, Q.L. Vuong, A. Roch, Magnetic resonance relaxation properties of superparamagnetic particles, WIREs Nanomed. Nanobiotechnol. 1 (2009) 299–310.
[6] A. Roch, R.N. Muller, P. Gillis, Theory of proton relaxation induced by superparamagnetic particles, J. Chem. Phys. 110 (11) (1998) 5403–5411.
[7] R.A. Brooks, F. Moiny, P. Gillis, On T2-shortening by weakly magnetized particles: the chemical exchange model, Magn. Reson. Med. 45 (2001) 1014–1020.
[8] P. Gillis, F. Moiny, R.A. Brooks, On T2-shortening by strongly magnetized spheres: a partial refocusing model, Magn. Reson. Med. 47 (2002) 257–263.
[9] S. Laurent, D. Forge, M. Port, A. Roch, C. Robic, L. Vander Elst, R. Muller, Magnetic iron oxide nanoparticles: synthesis, stabilization, vectorization, physicochemical characterizations, and biological applications, Chem. Rev. 108 (2008) 2064–2110.
[10] D.E. Sosnovik, R. Weissleder, Emerging concepts in molecular MRI, Curr. Opin. Biotechnol. 18 (2007) 4–10.
[11] J.H. Park, G. von Maltzahn, L. Zhag, M.P. Schwartz, E. Ruoslahti, S.N. Bhatia, M.J. Sailor, Magnetic iron oxide nanoworms for tumor targeting and imaging, Adv. Mater. 20 (9) (2008) 1630–1635.
[12] Y. Gossuin, S. Dish, Q.L. Vuong, P. Gillis, R.P. Hermann, J.H. Park, M.J. Sailor, NMR relaxation and magnetic properties of superparamagnetic nanoworms, Contrast Media Mol. Imaging 5 (6) (2010) 318–322.
[13] J.-F. Berret, A. Sehgal, M. Morvan, O. Sandre, A. Vacher, M. Airiau, Stable oxide nanoparticle clusters obtained by complexation, J. Colloid Interf. Sci. 303 (2006) 315–318.
[14] C. Sanson, O. Diou, J. Thévenot, E. Ibarboure, A. Soum, A. Brûlet, S. Miraux, E. Thiaudière, S. Tan, A. Brisson, V. Dupuis, O. Sandre, S. Lecommandoux, Loaded magnetic polymersomes: theranostic nanocarriers for MR imaging and magneto-chemotherapy, ACS Nano 5 (2) (2011) 1122–1140.
[15] B.A. Larsen, M.A. Haag, N.J. Serkova, K.R. Shroyer, C.R. Stoldt, Controlled aggregation of superparamagnetic iron oxide nanoparticles for the development of molecular magnetic resonance imaging probes, Nanotechnology 19 (2008) 265102–265108.
[16] A.M. Rad, A.S. Arbab, A.S.M. Iskander, Q. Jiang, H. Soltanian-Zadeh, Quantification of superparamagnetic iron oxide (SPIO)-labeled cells using MRI, J. Mag. Reson. Imaging 26 (2007) 366–374.
[17] Y. Gossuin, P. Gillis, R.N. Muller, A. Hocq, Relaxation by clustered ferritin: a model for ferritin-induced relaxation in vivo, NMR Biomed. 20 (8) (2007) 749–756.
[18] N.R. Ghugre, T.D. Coates, M.D. Nelson, J.C. Wood, Mechanisms of tissue-iron relaxivity: nuclear magnetic resonance studies of human liver biopsy specimens, Magn. Reson. Med. 54 (2005) 1185–1193.
[19] A. Roch, Y. Gossuin, R.N. Muller, P. Gillis, Superparamagnetic colloid suspensions: water magnetic relaxation and clustering, J. Magn. Magn. Mater. 293 (2005) 532–539.
[20] Y. Matsumoto, A. Jasanoff, T2 relaxation induced by clusters of superparamagnetic nanoparticles: Monte Carlo simulations, Magn. Reson. Imaging 26 (2008) 994–998.
[21] K.A. Brown, C.C. Vassiliou, D. Issadore, J. Berezovsky, M.J. Cima, R.M. Westervelt, Scaling of transverse nuclear magnetic relaxation due to magnetic nanoparticle aggregation, J. Magn. Magn. Mater. 322 (2010) 3122–3126.
[22] A. Abragam, Thermal relaxation in liquids and gases, in: The Principles of Nuclear Magnetism, Oxford University Press, Oxford, 1961, pp. 264–340.
[23] R.J.S. Brown, Distribution of fields from randomly placed dipoles: free-precession signal decay as result of magnetic grain, Phys. Rev. 121 (1961) 1379–1382.
[24] D.A. Yablonskiy, E.M. Haacke, Theory of NMR signal behavior in magnetically inhomogeneous tissues: the static dephasing regime, Magn. Reson. Med. 32 (1994) 749–763.
[25] T.J. Swift, R.E. Connick, NMR-relaxation mechanisms of O17 in aqueous solutions of paramagnetic cations and the lifetime of water molecules in the first coordination sphere, J. Chem. Phys. 37 (2) (1962) 307–319.
[26] J.L. Boxerman, L.M. Hamberg, B.R. Rosen, R.M. Weisskoff, MR contrast due to intravascular magnetic susceptibility perturbations, Magn. Reson. Med. 34 (1995) 555–566.
[27] R.P. Kennan, J. Zhong, J.C. Gore, Intravascular susceptibility contrast mechanisms in tissues, Magn. Reson. Med. 31 (1994) 9–21.
[28] A.P. Pathak, B.D. Ward, K.M. Schmainda, A novel technique for modeling susceptibility-based contrast mechanisms for arbitrary microvascular geometries: the finite perturber method, NeuroImage 40 (2008) 1130–1143.
[29] F. Lo Bue, F. Moiny, P. Gillis, Magnetic resonance susceptibility contrast induced by capillaries: a numerical comparison of two models, Magn. Reson. Mater. Phys., Biol. Med. 5 (1997) 39–44.
[30] A.L. Sukstanskii, D.A. Yablonskiy, Gaussian approximation in the theory of MR signal formation in the presence of structure-specific magnetic field inhomogeneities. Effects of impermeable susceptibility inclusions, J. Magn. Reson. 167 (2004) 56–67.
[31] V.G. Kiselev, S. Posse, Analytical theory of susceptibility induced NMR signal dephasing in a cerebrovascular network, Phys. Rev. Lett. 81 (25) (1998) 5696–5699.
[32] M.G. Shapiro, T. Atanasijevic, H. Faas, G.G. Westmeyer, A. Jasanoff, Dynamic imaging with MRI contrast agents: quantitative considerations, Magn. Reson. Imaging 24 (2006) 449–462.
[33] R.K. Wangsness, Magnetism in the presence of matter, in: Electromagnetic Fields, John Wiley & Sons, USA, 1979, pp. 351–390.
[34] D. Forge, Y. Gossuin, A. Roch, S. Laurent, L. Vander Elst, R.N. Muller, Development of magnetic chromatography to sort polydisperse nanoparticles in ferrofluids, Contrast Media Mol. Imaging 5 (3) (2010) 126–132.
[35] X. Xie, C. Zhang, Controllable assembly of hydrophobic superparamagnetic iron oxide nanoparticle with mPEG-PLA copolymer and its effect on MR transverse relaxation rate, J. Nanomater., 2011 (7p).